Dual-axis STEM tomography at 200 kV: Setup, performance, limitations

Reinhard Rachel[a],[*], Paul Walther[b], Christine Maaßen[c], Ingo Daberkow[d], Masahiro Matsuoka[e], Ralph Witzgall[c],[*]

[a] *Center for Electron Microscopy, University of Regensburg, Regensburg, Germany*
[b] *Central Facility for Electron Microscopy, Ulm University, Ulm, Germany*
[c] *Institute for Molecular and Cellular Anatomy, University of Regensburg, Regensburg, Germany*
[d] *TVIPS GmbH, Gauting, Germany*
[e] *JEOL GmbH, Freising, Germany*

ARTICLE INFO

Keywords:
Electron tomography
STEM tomography
Dual-axis tomography

ABSTRACT

The interpretation of cell biological processes hinges on the elucidation of the underlying structures. Their three-dimensional analysis using electron tomography has extended our understanding of cellular organelles tremendously. The investigations depend on the availability of appropriate instruments for data recording. So far, such investigations have been done to a great extent on 300 keV transmission electron microscopes. Here we show the implementation of STEM tomography on a 200 kV FEG transmission electron microscope, including the tuning of the condenser for forming a beam with a small illumination aperture, dual-axis data recording, and evaluation of the maximum sample thickness and quality of the data. Our results show that the approach is accomplishable and promising, with high reliability, and reaching excellent data quality from plastic sections with a thickness of at least 900 nm.

1. Introduction

Despite the arrival of super-resolution fluorescence microscopy, electron microscopy in its various forms remains the mainstay of ultrastructural research. Whereas the first technique depends on the use of fluorescent molecules and offers a resolution of 20 to 50 nm, only the latter is capable of visualizing cellular details without additional genetic tools and at the required resolution of 5 nm (the width of a lipid bilayer) and better. Just like any imaging technique, however, electron microscopy is confronted with the challenge of providing information in three spatial dimensions. Developments over the past years such as electron array tomography (Markert et al., 2016; Micheva and Smith, 2007), serial block face-scanning electron microscopy (Denk and Horstmann, 2004), focused ion beam-scanning electron microscopy (Burghardt et al., 2015) and electron tomography (Frank, 1992) help to overcome this problem.

Electron array tomography and serial block face-scanning electron microscopy represent comparatively low resolution approaches because they are based on the sectioning of a specimen with a diamond knife. In electron array tomography, a ribbon of sections is placed on a carrier and then imaged by scanning electron microscopy, whereas in serial block face-scanning electron microscopy it is the tissue block which is scanned after each section with the section being discarded. Owing to the underlying technique, the resolution only lies in the range between 50 and 100 nm in the *z* axis, but it is possible to cover a large range in *z* (up to 20 μm). The principle of focused ion beam-scanning electron microscopy is similar to that of serial block face-scanning electron microscopy except that the specimen is trimmed by a gallium beam which repetitively mills away a thin (~5–15 nm) layer of the plastic-embedded tissue. Since the milling and imaging steps can be automated, it is again possible to obtain three-dimensional information over a large range (at least 10 μm) but at a higher resolution in the *z* axis. Finally, electron tomography offers the highest resolution in the *z* axis (~5 nm, depending on the sample preparation, the tilt scheme, and the reconstruction) but it suffers from the disadvantage that only a small portion of the section can be imaged. Therefore electron tomography will represent the method of choice if a cell biological question with a focus on a small subcellular volume, e.g. concerning the centrosome or the Golgi apparatus, has to be answered.

In electron tomography, a grid with a 100–900 nm thick section is tilted relative to the electron beam, typically between up to −72° to +72°. Tilted projections are acquired at either equal angular increments or employing the Saxton protocol (Saxton et al., 1984). Obviously, the electrons will have to travel a longer distance through the

section the more the specimen is tilted (more than three times the thickness at a tilt angle of 72° compared to a non-tilted specimen), which entails several problems. Electrons will be scattered in the sample, either elastically or inelastically. In the latter case the electrons lose energy thus resulting in chromatic aberration in the objective lens and ultimately to blurring of a TEM image. This effect increases with increasing specimen thickness and in the case of tomography also with increasing tilt angles.

Another restricting parameter is the limited depth of focus in transmission electron microscopy (TEM) which is a problem with thick sections and even more so with sections imaged at high tilt. A typical field width of the image amounts to 2.74 μm in our setup (2048 pixels × 1.34 nm pixel size). When considering a section thickness of 440 nm, the edges of the section in the *z* direction lie 2.75 μm apart at a tilt angle of 72°, which restricts the useful thickness of a section in TEM tomography. It is, however, less of a limitation in STEM tomography as explained below. The main advantage of STEM imaging lies in the prevention of chromatic aberration. Since there are no image forming lenses between sample and STEM detector, chromatic aberration is not an issue and also inelastically scattered electrons can contribute to image formation. As already shown over a decade ago (Aoyama et al., 2008), STEM tomography is also superior to energy-filtered TEM tomography, since all electrons (unscattered and scattered) contribute to image formation, whereas in energy-filtered TEM tomography only electrons within a small energy range can be used for image formation and therefore most of the electrons are lost. It was also shown that for geometrical reasons the signal from the bright-field detector provides better resolution from the depth of a thick (e. g. 1 μm) section (Hohmann-Marriott et al., 2009; Sousa et al., 2011).

When imaging thick biological samples in STEM mode, two factors need to be kept in mind concerning the ultimate sample thickness which can be imaged in focus. One limiting parameter results from the geometry of the illuminating beam and affects the depth of focus, the other parameter is due to the scattering of the primary beam. The depth of focus in the sample can be optimized by a small convergence angle of the primary beam, in modern instruments it can be kept below 10 mrad irrespective of the voltage (Biskupek et al., 2010). Alternatively, dynamic focusing can be applied when the sample is tilted so that the focus of the electron beam follows a given plane within the tilted sample. Furthermore, the resolution of the imaging system is limited by the fact that the beam is increasingly scattered when traversing the sample, thus resulting in a beam-broadening effect (Hohmann-Marriott et al., 2009). This effect reduces the resolution in the lower parts of the sample volume and is slightly more pronounced at a lower voltage of the primary beam (e.g. 200 *vs*. 300 kV) (Walther et al., 2018).

A number of STEM tomography studies were performed at 300 kV, others at 200 kV. Pilot projects, performed on 300 kV microscopes, focused on the beam forming system and the image recording (Biskupek et al., 2010; Sousa et al., 2011) which resulted in the investigation of human hemophagocytes (Biskupek et al., 2010), pancreatic beta cells (Sousa et al., 2011), and virus-infected cells (Schauflinger et al., 2013). Later, a number of studies were performed also at 200 kV, investigating e.g. the infection cycle of the giant mimivirus (Mutsafi et al., 2013), plastoglobuli in the halotolerant algae *Dunaliella bardawil* (Davidi et al., 2014), damaged mitochondria in HeLa cells (Ader and Kukulski, 2017), the cilia transition zone in the flagellate *Trypanosoma brucei* (Trépout et al., 2018), plant thylakoid ultrastructure (Bussi et al., 2019), whole bacterial cells, lamellipodia of osteosarcoma cells, and mitochondrial matrix granules using cryoSTEM tomography (Wolf et al., 2017, 2014). As early as 2012, Leapman noted that "STEM tomograms of thick sections present a level of ultrastructural detail similar to that which can be observed by conventional ET on sections of intermediate thickness (300–400 nm)" (Sousa and Leapman, 2012). Despite the obvious advantages of STEM tomography, the sites where this technique is used to image thick biological samples seems to be rather limited.

In the current study we describe a protocol which facilitates the switch of TEM to STEM imaging for tomography. We provide a detailed guideline how a 200 kV transmission electron microscope with a field emission gun can be successfully converted to a 200 kV STEM microscope for biological applications using an electron beam with small semi-convergence angle. The illumination concept is similar to that in STEM nanodiffraction experiments (Alloyeau et al., 2008; Ganesh et al., 2010) resulting in a high depth of focus. Together with optimization of the rest of the imaging system and a powerful software, single- and dual-axis STEM tomography datasets from plastic-embedded samples with a maximum thickness of up to 900 nm can be recorded routinely with high consistency and reproducibility. Moreover, we demonstrate that our data are of a high enough quality for semi-automated reconstruction using the IMOD software package, thus increasing the throughput of samples and yielding a large amount of high-quality three-dimensional data.

2. Results

2.1. Comparison between TEM tomography and STEM tomography

We conducted a simple experiment in order to compare electron micrographs obtained in regular transmission electron microscopy (TEM) and in scanning transmission electron microscopy (STEM) mode. To this end, kidney sections of 100 nm, 300 nm and 900 nm thickness were imaged at 200 kV in an electron microscope with a field emitter as an electron source. It can be seen that the image quality, as judged from the visibility of sample details, is superior in STEM bright-field images in comparison to that of regular TEM images (Fig. 1). In addition, we were curious to see how an 800 nm thick kidney section can be visualized by STEM imaging (illumination with small convergence angle) at a low magnification. Such an image provided an overview and showed the superior presentation, in particular in dark-field mode (suppl. Fig. 1) where e.g. all microvilli are in focus although they are not lying in the same plane of the specimen. The high depth of focus is of advantage for visualizing such a specimen and for the identification of a region of interest.

2.2. Optimization of STEM tomography

Recording tomography data in STEM mode using a beam with small convergence angle at 200 kV shows all the advantages described for STEM imaging at 300 kV under similar conditions (Biskupek et al., 2010). We want to emphasize two beneficial effects in particular. Firstly, two signals are recordable simultaneously, i.e. bright-field and dark-field images (suppl. Fig. 2; (Sousa et al., 2011; Walther et al., 2018)). Secondly, images are sharp in all areas, although the electron beam has to travel a longer path through the sample at high tilt: 2.46 times at 66° tilt, 3.24 times at 72° tilt (Fig. 2a–d, suppl. Figs. 2 and 3). On the other hand, image recording is inherently slower in STEM than in TEM mode. About four images per minute are recorded in TEM tomography in our setup but only about one image per minute using STEM tomography. This includes additional images for tracking and focusing at each tilt angle. Initially a STEM tomography series of 145 projections with a 1° linear increment (−72° to +72° tilt angle) lasted ~155 min (including tracking, focusing and recording). Later we reduced the time to ~100 min for 90 projections with a 2° increment (−66° to +66° tilt angle) according to the Saxton scheme (Saxton et al., 1984). By comparison, recording TEM tomograms with the same scheme those 90 projections only took ~30 min on the same instrument. Accordingly we are able to record 10 to 15 tomograms in TEM mode but only up to three tomograms in STEM mode in a 9-hour working day because time in addition to the actual tomography is needed for preparatory measures such as setting up the instrument, searching for suitable specimen areas and pre-exposure (beam shower) of the region of interest in order to stabilize the section. Obviously the design of the tilt scheme matters. In our studies we found that recording
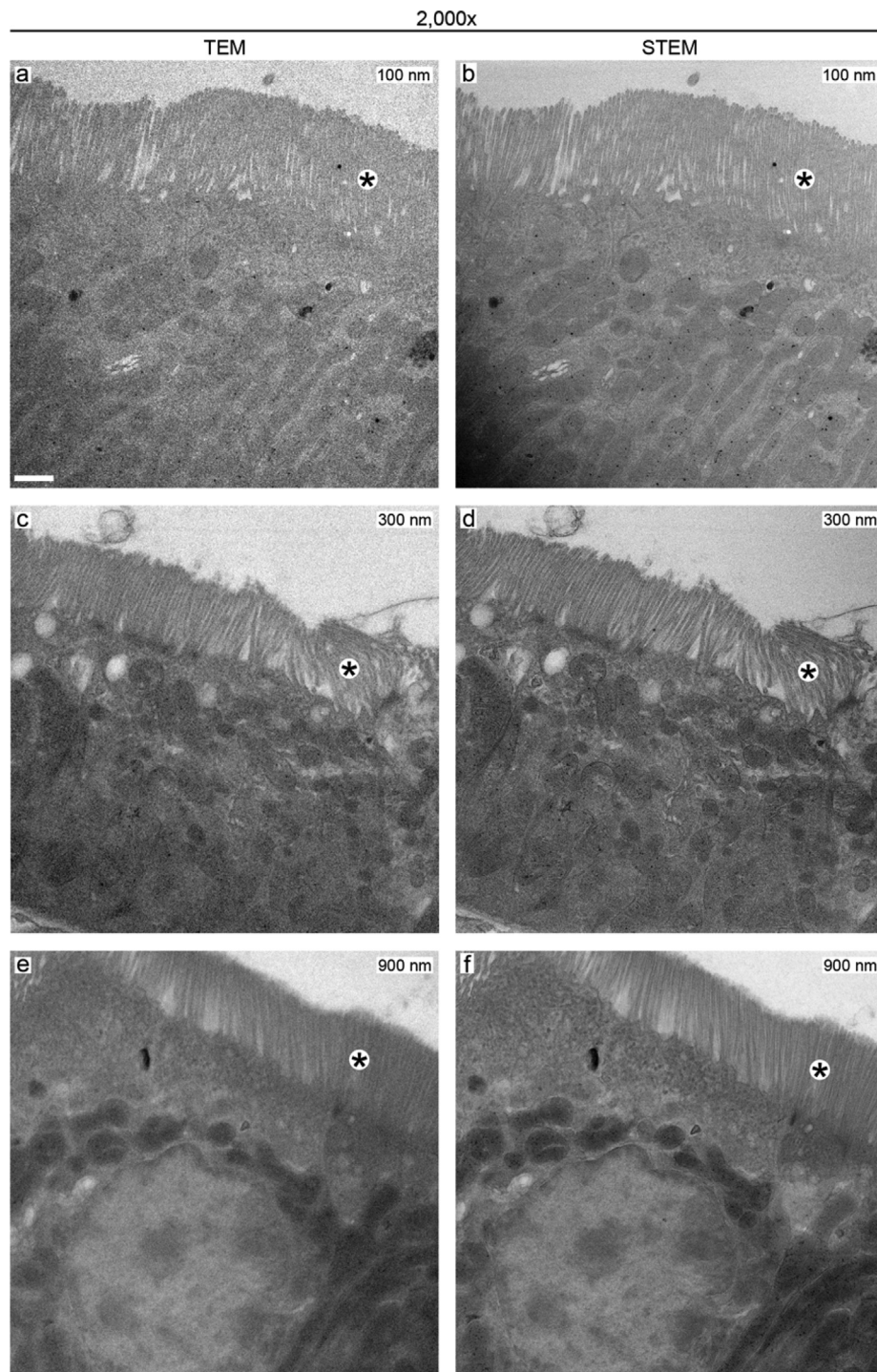
Fig. 1. Side-by-side comparison of TEM and STEM bright-field images. Identical areas of an Epon-embedded murine kidney section were visualized at nominal magnifications of 2,000x and 8,000x by transmission electron microscopy (TEM) and scanning transmission electron microscopy (STEM). Whereas at 2,000x magnification, differences between TEM and STEM pictures were minor in the case of 100 nm thick sections (a, b), they became more apparent for 300 nm (c, d) and even more so for 900 nm thick sections (e, f). The image quality was better for all sections at 8,000x magnification when data were recorded in STEM modus (g–l). The brush border of the proximal tubule is indicated by an asterisk. All data were acquired at 200 kV. In the case of TEM, the electron dose was estimated to be ~10 electrons/nm^2 and ~100 electrons/nm^2 for 2,000x and 8,000x magnification, respectively. For STEM images, the dose was ~5 times higher. Bar, 1 μm (a-f), 500 nm (g–l).

datasets at 2° linear increments was too coarse. Specifically, the signals emerging from the gold fiducials in the reconstructed volume (typically visible as a striped pattern) interfered with the information contained in the biological sample itself. This effect can be reduced by the "gold erasing" feature implemented in IMOD. Tomograms with 1° linear increments yielded somewhat more detailed tomograms but took

considerably more time (almost twice as much) to be recorded. This problem was resolved by employing a 2° increment protocol as formulated by Saxton (implemented in EM-TOOLS) in which projections are collected every ~2° at low tilt angles and every ~0.8° at high tilt angles. We thereby obtained fully satisfactory datasets which were indistinguishable from data recorded at linear 1° increments.
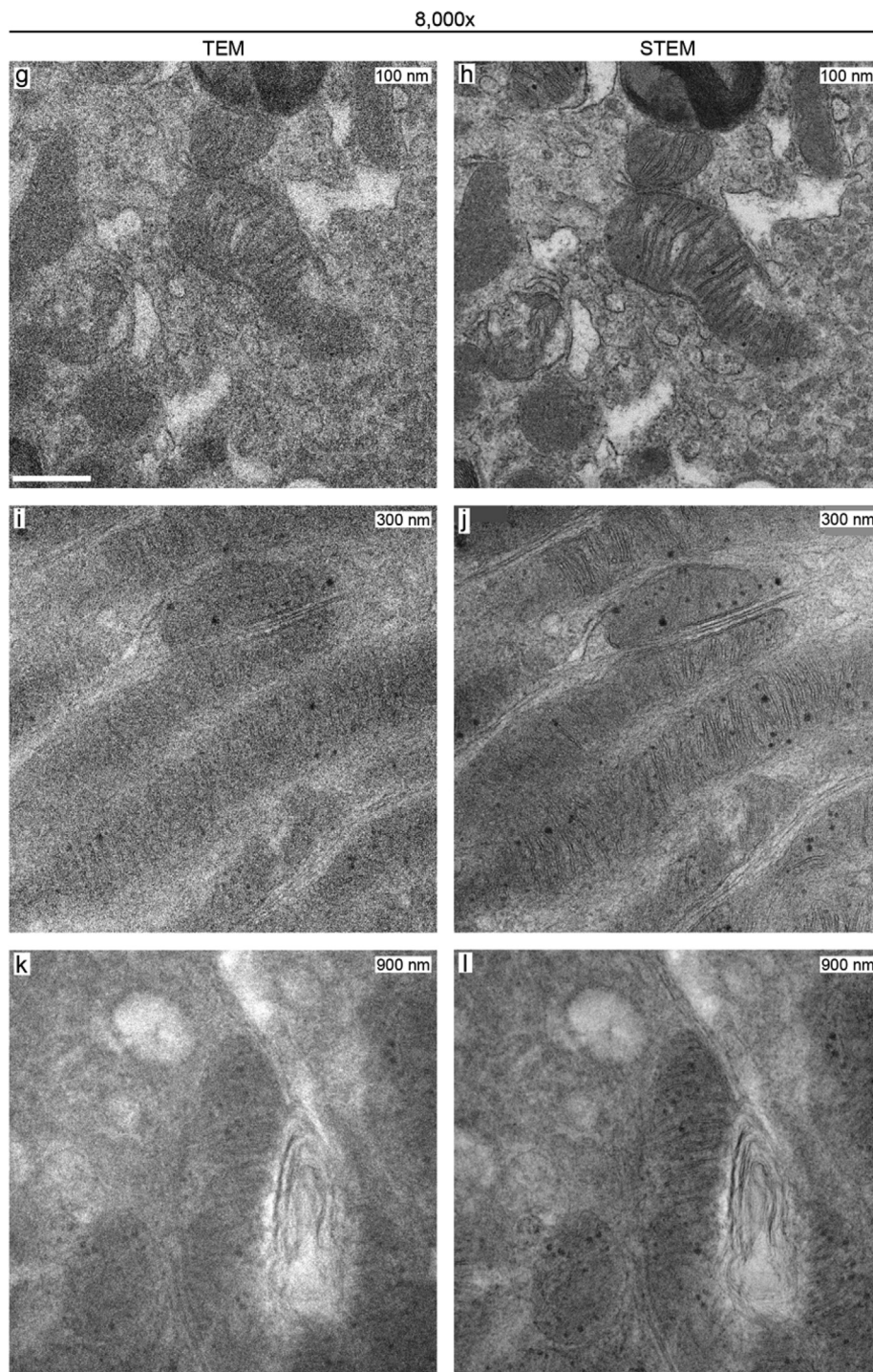
Fig. 1. (*continued*)

When recording data from sections as thick as 900 nm in TEM mode, the identification of the correct focus, in particular of tilted samples, can be challenging (Fig. 2a, c). Only images at or near zero focus are interpretable, while already at low underfocus (Δf of −1,000 nm or higher) image details are blurred, which can make the interpretation of details difficult. Furthermore, the tracking of fiducials which are out of focus can be a problem. This is even more severe when recording TEM images at high tilt angles (in particular at angles between 60° and 66° or even 72°) (Fig. 2c). In STEM imaging with a small convergence angle, focusing is accomplished by recording five differently focused images and then determining the optimal focus using a sharpness function. In this mode, well-focused images are interpretable in all areas in the

bright-field (Fig. 2b, d, suppl. Fig. 2a, c) and dark-field channels (suppl. Fig. 2b, d), and even at the edges of high-tilt images (Fig. 2d, suppl. Fig. 2c, d). A comparison of images obtained at 0° and 66° tilt angle (Fig. 2b, d) demonstrates that all fiducials are clearly visible as dark spots of similar contrast in the recorded image area both along the tilt axis and a certain distance away from it. This is a direct consequence of the STEM imaging modus which contrasts with TEM imaging. At a high tilt angle in TEM, multiple electron scattering in the thick sample together with chromatic aberration results in blurred details, in particular on the edge of the image, thus making the visualization of gold fiducials difficult or impossible (Fig. 2c). The improved image quality in STEM mode is also reflected in the 3D reconstruction independent of the
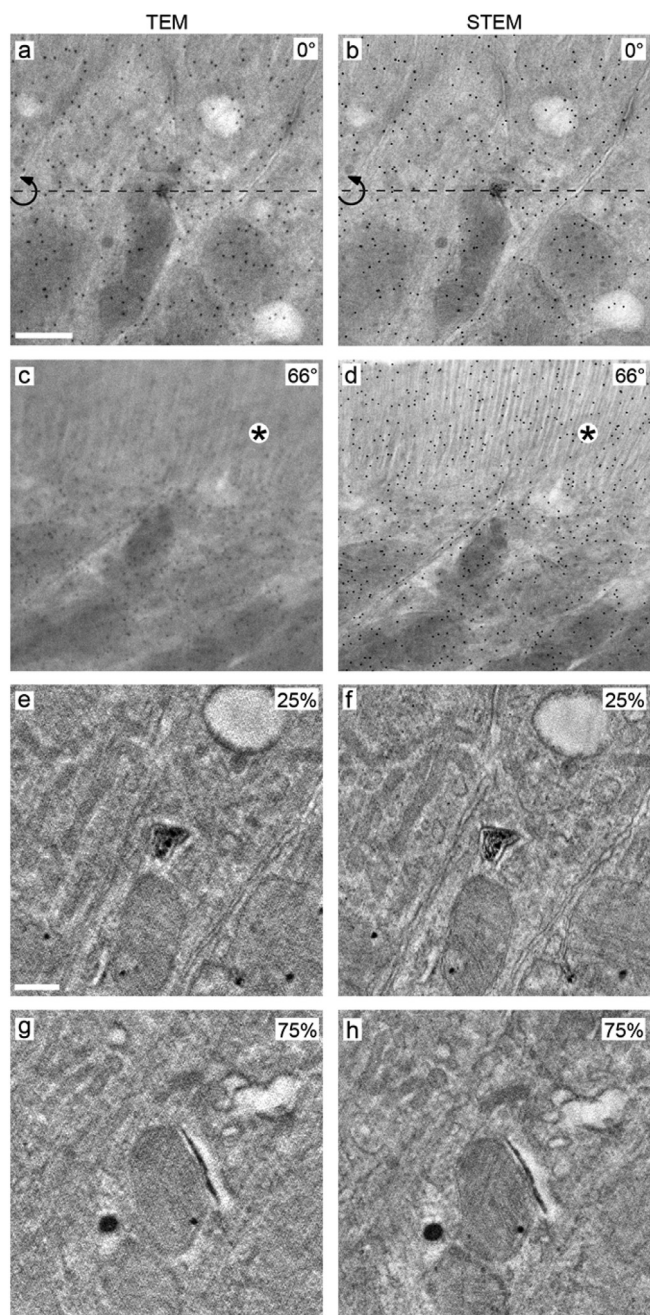
Fig. 2. Side-by-side comparison of TEM and STEM tomograms. A nominally 800 nm thick section of an Epon-embedded murine kidney sample was tomographed by transmission electron microscopy (TEM) and scanning transmission electron microscopy (STEM). The original bright-field images shown were obtained at 0° and 66° tilt angles (a–d), the tilt axis is indicated by a dashed line (a, b). In the reconstruction (e-h), a comparison of slices at 25% and 75% of section thickness demonstrates the superior data quality obtained by STEM tomography. An individual slice was 2.7 nm thick. The brush border of the proximal tubule is indicated by an asterisk. All data were acquired at 200 kV. The section was first pre-irradiated at a dose of ~200,000 electrons/nm^2, then the TEM tomography data and finally the STEM tomography data were acquired. In the case of TEM tomography, the dose of an individual image was ~330 electrons/nm^2 and for the full dataset ~30,000 electrons/nm^2. In the case of STEM tomography, the dose of an individual image was ~1,800 electrons/nm^2 and for the full dataset ~162,000 electrons/nm^2. Bar, 500 nm (a-d), 250 nm (e-h).

algorithm used, be it the weighted back projection (WBP) protocol or the simultaneous iterative reconstruction technique (SIRT). Structural details in the sample are resolved better in the STEM tomogram (Fig. 2f,

h) when directly compared to the identical slices in the TEM tomogram (Fig. 2e, g).

When checking the visibility and in particular the intensity of the gold fiducials in STEM bright-field images (Fig. 3, suppl. Fig. 2), gold fiducials were recognizable either as sharp dots or as slightly blurred ones even without tilting the sample (Fig. 3a, b). Direct comparison of high-tilt data with the 0° image and with the 3D reconstruction revealed that the sharp gold fiducials reflect those lying on top of the section, while the slightly blurred ones reflect those at the bottom of the section (Fig. 3c–f, suppl. Fig. 3). We believe that this difference results from two effects. For one, the electron beam is broadened due to the scattering of the electrons within the sample, and secondly the electron beam has a small but noticeable convergence angle, and therefore a limited depth of focus. As we have seen this effect in all our datasets recorded, with samples of varying thickness and slightly varying defocus settings, we assume that the contribution of the beam broadening is by far dominating. This is supported by earlier observations (Hohmann-Marriott et al., 2009), see also chapter 5 in (Reimer and Kohl, 2008).

The reconstruction of a single-axis tilt series using IMOD shows a clear definition of structural features in the *z* axis, indicating that the data are well defined (Fig. 4, suppl. Figs. 4, 5). This nominally 800 nm thick section turned out to be 620 nm thick after initial pre-exposure and subsequent irradiation during tomography. This corresponds to a shrinkage by ~22%, similar to what has been described before (Luther, 2006). The sample shows well demarcated microvilli of the brush border in renal proximal tubules (shown in suppl. Fig. 4 in four representative *x-y* views). In the *x-z* and *y-z* planes, the microvilli comprising the brush border of the proximal tubules are well discernible in longitudinal and cross sections in most cases. The plasma membrane, however, cannot be fully traced in the case of microvilli oriented horizontally which is caused by the missing wedge effect in single-axis tilt series.

In order to minimize the missing wedge, we imaged the same region by dual-axis STEM tomography (Bussi et al., 2019; Mastronarde, 1997; Sousa et al., 2011). We encountered no problems recording data in either orientation from the same region of interest, in particular no further shrinkage was observed. The general appearance of the sample after dual-axis reconstruction (suppl. Fig. 4) is clearly improved in a noticeable manner since more details are visible. The appearance of horizontally oriented microvilli is considerably sharpened (Fig. 4), and this is clearly visible in all three planes. Specifically, whereas the number and distinct outline of individual microvilli can barely be determined in the single-axis reconstruction (Fig. 4a-d), the microvilli and their membranes are clearly visible in the dual-axis reconstruction and thus the number of microvilli is easy to count (Fig. 4e-h). Some microvilli which were barely visible by single-axis tomography were clearly identified by dual-axis tomography (Fig. 4). The plasma membranes of the cell body and of the microvilli are perfectly traceable in both the *x-y* and *x-z* view by dual-axis data recording (suppl. Fig. 5).

2.3. Reconstruction strategies

Data recorded by STEM tomography were easy and straightforward to process using IMOD. The high contrast and the improved visibility of gold fiducials at all tilt angles turned out to be valuable during the alignment process, and this helped to obtain high-quality 3D reconstructions in a reliable manner. Therefore we tested to which extent we could process the data using the recently published automated alignment and reconstruction pipeline in IMOD (Mastronarde and Held, 2017). Seeding and tracking of fiducials was done using standard parameters without any user intervention, which turned out to be robust and reliable. Tracking was regularly possible up to a tilt angle of ~55°, and for many fiducials even up to 66°, the highest tilt angle at which we routinely recorded tomograms. The option to use the automated alignment tool depended on the thickness of the section and on
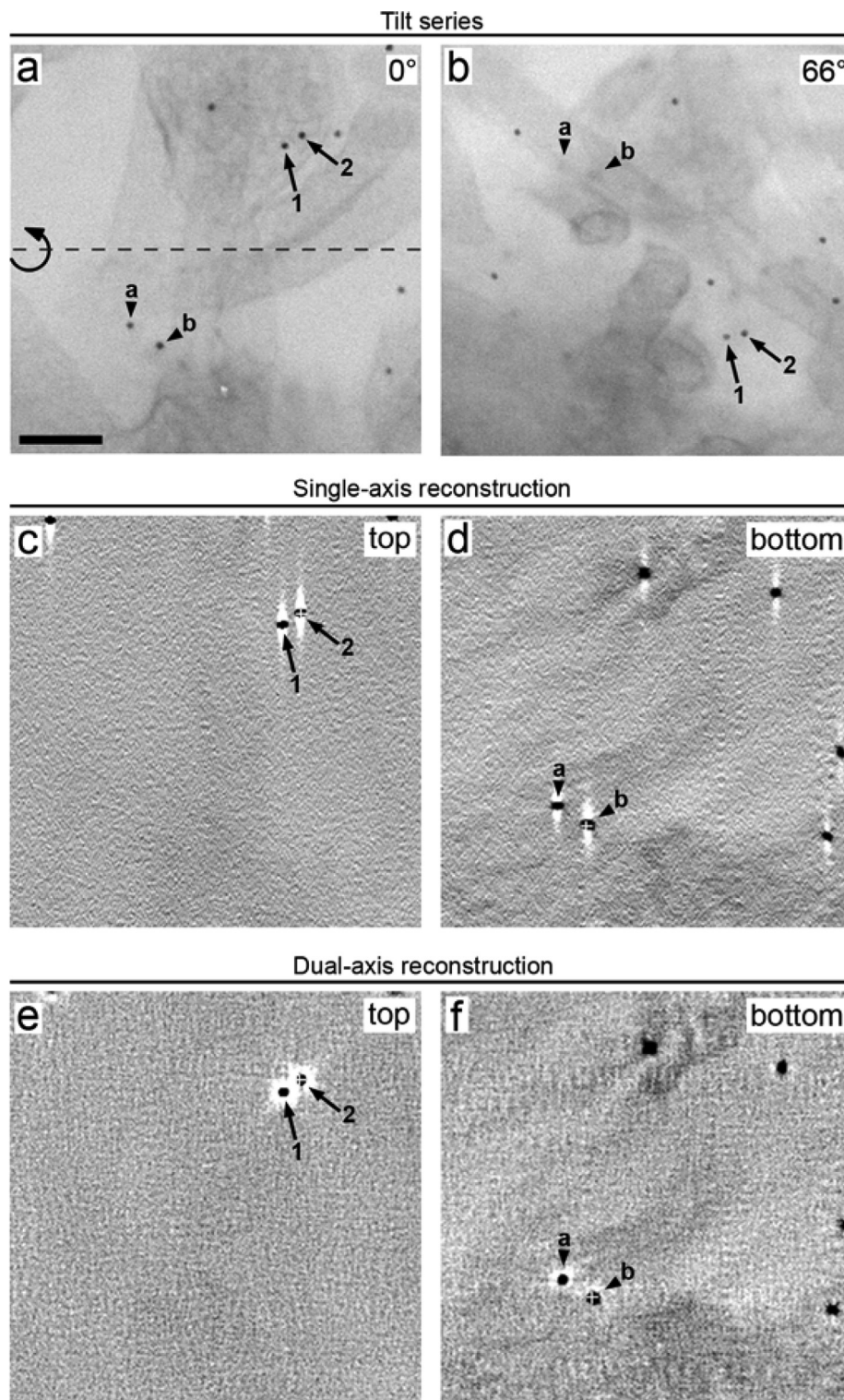
Fig. 3. Imaging of gold fiducials. A nominally 800 nm thick section of an Epon-embedded murine kidney sample was subjected to STEM tomography, the tilt axis is indicated by a dashed line (a). Gold fiducials with a diameter of 15 nm were applied both to the top and bottom of the section. While at 0° tilt angle both populations of gold fiducials are visible (a), at a large tilt angle only those fiducials on the top side of the section are still clearly visible (1, 2 in panel b) whereas those on the bottom side of the section are blurred (a, b in panel b). Furthermore, it can be seen that a dual-axis tilt series leads to less artefacts as evidenced by the round halos around the gold particles (e, f) in comparison to the elongated halo after a single-axis tilt series (c, d). All data were acquired at 200 kV. Bar, 200 nm.

the visibility of the signal arising from a gold fiducial. The tracking of fiducials was possible throughout the section when fiducials lay on pure resin without any additional cellular or tissue components. However, in the case of sections containing biological samples contrasted with heavy metals (in our case uranyl acetate and OsO_4) we observed occasional failures in tracking the fiducials, starting at a tilt angle above ~55°. At this stage user intervention was necessary to optimize tracking of the fiducials. For some of our samples automated tomogram positioning was not reliably achieved due to their low contrast. The default parameters in IMOD for plastic-embedded samples are not (yet) able to

robustly detect the sample if – as in some samples – extended areas with "empty resin" are present. The built-in option "cryo positioning" for samples with low contrast also failed, therefore user intervention is still essential for a successful outcome.

In order to test the limits of STEM tomography on an additional biological specimen we wanted to reconstruct a complete basal body *plus* the surrounding structures in a single tomogram. Retinal pigment epithelial cells were high-pressure frozen, freeze-substituted and embedded in Epon, then 900 nm thick sections were prepared. At 0° (Fig. 5a) and 66° the gold fiducials were as easily detectable as
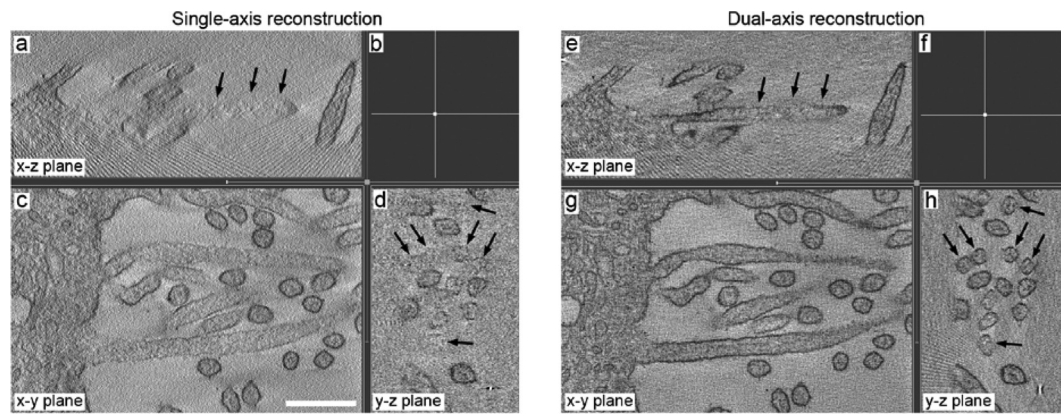
Fig. 4. Comparison of STEM single-axis and dual-axis tomography. A nominally 800 nm thick section of an Epon-embedded murine kidney sample was subjected to single- and dual-axis STEM tomography, with a focus on the brush border. It can be easily appreciated that some microvilli were only visible in the dual-axis tilt series (compare arrows in a and e, and d and h, respectively). Panels b and f indicate the position of the slices in the reconstructed volume. Bar, 200 nm.

described above which made it possible to perfectly focus at all tilt angles. After beam showering the sample and recording the tilt series the section turned out to be 720 nm thick which amounts to a comparable decline in the thickness of the sample as noted above. The data were reconstructed using the WBP algorithm including a SIRT-like filter. Numerous details can easily be identified in selected slices of the reconstructed dataset such as microtubules, ribosomes, mitochondria, multi-vesicular bodies and a daughter centriole (Fig. 5b, c). When comparing this result to a reconstruction obtained by using the pure SIRT algorithm, the visual outcome was virtually indistinguishable but obtained at the expense of a longer computing time in the case of the SIRT protocol. It was gratifying to see that we were able to visualize both the mother and the daughter centriole in a single ~900 nm thick sections, this was not possible in 300 nm sections.

2.4. Optimization

When recording STEM tomograms, it became obvious that the time for focusing occupied a considerable portion (~one third) of the total recording time. During each series the software EM-TOOLS tracks the movement of the sample in the *x*, *y* and *z* directions (output for *z*: Fig. 6a). After having taken a closer look at many of those data it became clear that in more than 50% of the tomograms the total movement in the *z* direction, reflected by a change of the focus, was in the range of 1.5 μm or even smaller, it rarely exceeded 2 μm. Since the depth of focus in STEM tomography using a beam with a small convergence angle is in the range of 5 μm and higher (Biskupek et al., 2010) we wondered whether focusing was necessary at all. We set up two tomography series, one with and the other without automated focusing. Both at 0° tilt angle and at 66° tilt angle (and at all other tilt angles, not shown here), the images of both series were virtually indistinguishable from each other (Fig. 6b-e). Therefore, automated focusing is dispensable for most specimens and it is possible to increase the daily number of tomograms to 5 per 9 h-working day. Another problem is that for some specimens, in particular for sections on plastic films mounted on 1 × 2 mm slot grids, the images may become blurred in particular at high tilt angles, possibly due to movement of the section in the z direction. If an easy protocol could be developed to assert the flatness of the specimen this would allow a considerable increase in the number of tomograms.

3. Discussion

We have demonstrated that STEM tomography using an electron beam with a small convergence angle can be carried out on a 200 kV transmission electron microscope. The results obtained are highly superior to those achieved by regular TEM tomography. Due to the visibility of the gold fiducials in all parts of the recorded images at almost all tilt angles, the tomogram can be easily reconstructed manually, and in many cases the automated reconstruction algorithm in IMOD can be employed (Mastronarde and Held, 2017). We have recorded numerous single-axis tomograms which are sufficient to answer the relevant questions (Hochapfel et al., 2018; Walther et al., 2018) but we also want to emphasize that dual-axis tomography helped to resolve more details in our samples, e.g. the lightly stained cell membranes lining microvilli. The additional recording time resulting from the second dataset certainly is worthwhile depending on the question being asked.

3.1. Time considerations

One drawback of STEM tomography is the rather long time it takes to set up the tomography and execute it. In order to increase the throughput and reduce the total cost, an electron microscope should ideally be operated without supervision overnight. This is now possible due to the use of large anti-contaminating devices and improved operating software. The recording time can be reduced using a brighter electron source such as a cold field emission gun (cFEG) or extra-bright FEG (XFEG). In this respect, we favor the performance of a cFEG for the following reasons. It is known that a cFEG ultimately has a five times smaller crossover size, a higher current density and a higher brightness compared with a Schottky field emitter (see Table 5.1 in (Williams and Carter, 2009)). Ideally, all this can be used to achieve an even smaller and brighter STEM probe of high brightness without a costly monochromator, thus enabling the recording of data with smaller pixel size (i.e., higher spatial resolution) and higher signal-to-noise ratio. A cFEG might also be a means to find ideal imaging conditions for low-dose STEM at high resolution (Buban et al., 2010) provided that new instruments are equipped with flexible control systems of the beam current and a scan system which is fast, free of distortions, scan noise and drift artefacts (Savitzky et al., 2018). Fast low-dose STEM imaging might also be achievable via new software controlling beam scanning and image acquisition (Mittelberger et al., 2018). Furthermore, bright-field and dark-field STEM detectors with higher sensitivity will shorten the time for individual images. Both a brighter electron source and improved detectors should help to reduce the time for recording the tilt series considerably. It would also be desirable to reduce the time for setting up the microscope for STEM, in particular including the illumination with a small convergence angle, using an automated workflow. Currently the setup of our electron microscope is done manually and includes careful adjustment of the electron optics and the goniometer, first by loading specific setting files and subsequently by
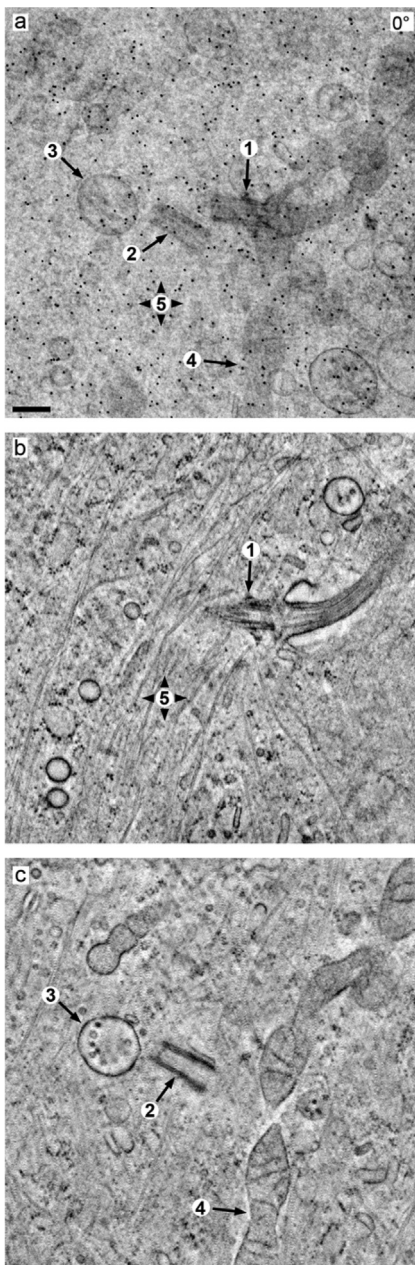
Fig. 5. Visualization of a primary cilium by STEM single-axis tomography. A nominally 900 nm thick section of an Epon-embedded human retinal pigment epithelial cell was subjected to single-axis STEM tomography. Panel a shows the bright-field image of the section, panels b and c show two selected slices of the reconstructed volume in which the basal body with its attached primary cilium (1), the daughter centriole (2), a multi-vesicular body (3), a mitochondrion (4) and cytoskeletal filaments (5) are easily detectable. Bar, 250 nm.

manual fine tuning. Regrettably, automation at this step is not available yet.

A considerable amount of time is needed for tracking the region of interest, this depends to a large extent on the precision of the goniometer. We routinely reconstruct an area of ~2.7 μm × 2.7 μm in the *x-y* plane by STEM tomography. However, due to the image shift observed upon tilting the sample the scanned area extends to ~4 μm × 4 μm in the *x-y* plane. A more accurate goniometer would enable us to scan and reconstruct larger regions of interest. Further improvement seems feasible by using a goniometer equipped with a piezo nano-positioning device which would be helpful in several aspects. First, the movement of the sample during the tilt series would be minimized in all three spatial directions, thus eliminating the need for time-consuming tracking and focusing. And second, an alternative possibility to low-dose focusing on a neighboring sample area would be opened, just a few μm away from the region of interest. This is useful because beam deflection in STEM mode is usually restricted to the area of interest and further deflecting the beam for low-dose focusing is not possible which represents an inherent restriction of the scanning unit in our electron microscope.

Another time-consuming part of STEM tomography results from the recording of many images during focusing as currently embedded in our routine. Focusing might be unnecessary because the depth of focus is large and therefore the movement of the sample in the *z* direction from one tilt angle to the next might be negligible as suggested by our initial tests. The large depth of focus is helpful to minimize the number of "focus" images at every tilt angle, as a compromise it may be sufficient to focus every 15° or 20°. This needs to be tested on a larger number of samples.

Finally, automated forwarding of the final tomography data onto dedicated workstations using scripts (for automated file transfer) and dedicated hardware for processing can yield a preliminary 3D reconstruction within minutes. This will make it possible to decide instantaneously whether the sample under investigation deserves more detailed imaging (e.g. via dual-axis tomography) for which an optimized setup of the microscope would be required. For instance, *Focus* provides an interface between data collection and image processing for cryo-transmission electron microscopy (Biyani et al., 2017).

3.2. Dose considerations

The dose for images taken in STEM mode in our study were ~5 times higher than in TEM mode (1,800 *vs.* 330 electrons/nm^2 for images; 162,000 *vs.* 30,000 electrons/nm^2 for tomography series). One might argue that the higher dose in STEM tomography used to record the data contributes to the better visibility of sample details. While we cannot rule out this possibility completely, we want to reemphasize that in STEM tomography we avoid chromatic aberration and gain a high depth of focus. This cannot be achieved in TEM mode through simply collecting more electrons. We ourselves have never attempted to reduce the dose in STEM tomography but it was first predicted by Hegerl and Hoppe (1976) and later shown by McEwen et al. (1995) that a fractionation of the total recorded dose while collecting 3D tomography data sets is indeed possible. A considerably lower dose (total number of 11,500 electrons/nm^2) was used e.g. in cryoSTEM-tomography (Wolf et al., 2014) using a three times larger pixel size (4 nm) in the individual STEM images, as compared to our data. A 1:1 comparison with our data is not straightforward because the samples in that study were unstained bacteria whereas we used samples stained with heavy metal atoms, furthermore camera lengths and STEM detectors were set in a different way.

3.3. Quality considerations

The magnification at which optimal STEM performance can be achieved is not as low as is desirable for biological samples. Our electron microscope is a dedicated high-resolution microscope which makes fine-tuning at STEM magnifications below 200,000x (nominal) difficult. For tissue or cell culture specimens, we would like to carry out STEM tomography at magnifications as low as 60,000x or even 20,000x (nominal magnification) (as shown in Fig. 1 and suppl. Fig. 1), at present this cannot be done with an optimal optical performance. In addition, very fast scanning (in order to reduce the dose per pixel) comes with streaking artefacts in the images, similar to what has been described before (Buban et al., 2010).

The diameter of the beam is ~4 nm (full width at half maximum, suppl. Fig. 6). Thus, we do not expect a resolution of better than 5 nm, realistically it will rather be in the 10 nm range (Rayleigh criteria;
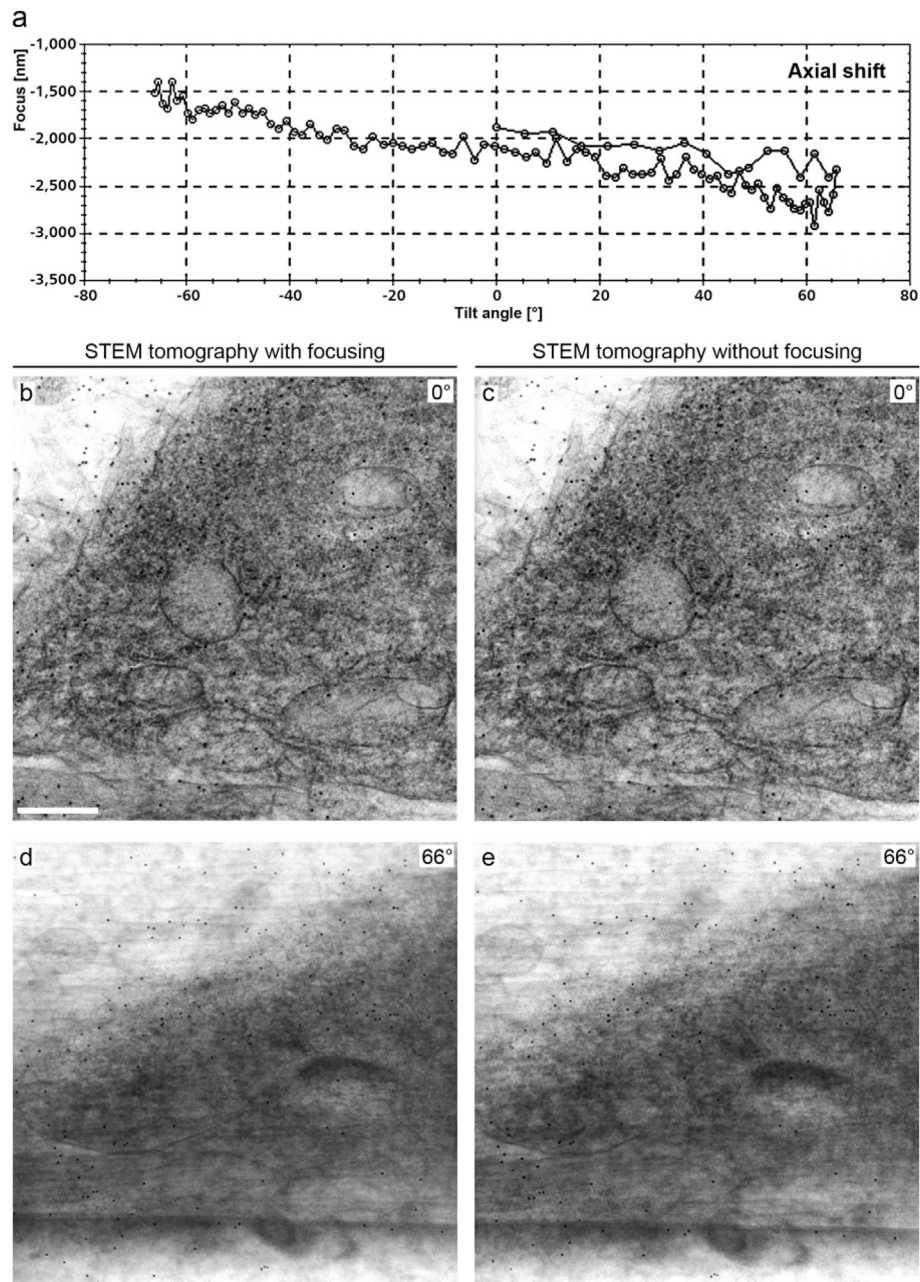
Fig. 6. STEM tomography with and without automatic focusing. A representative tilt series recorded by STEM tomography demonstrates that the shift of the focus plane does not exceed 1.5 μm (cf. the focus plane of −1,500 nm at −66° tilt angle and the focus plane of −2,900 nm shortly before the maximum tilt angle of + 66° in a). When the identical position was recorded with and without automatic focusing, the quality of the images was virtually identical as demonstrated by the bright-field images at 0° (b, c) and 66° tilt angle (d, e). Bar, 500 nm.

Biskupek et al 2010). The beam width can be reduced by using a smaller condensor aperture on the expense of the number of electrons. In the end, the beam diameter is mainly determined by the following parameters of the instrument, i.e. the probe-forming gun (a cFEG might be advantageous), the setting of the condensor minilens, and the focal length of the objective lens (the gap of the pole piece). Optically, a 200 kV instrument can perform as well as a 300 kV instrument, except for the greater penetration depth of the latter.

Some steps of the sample preparation need to be optimized for STEM tomography. The Humbel laboratory has demonstrated that the kind of resin influences the stability of the specimen during sectioning and extended electron beam irradiation (Kizilyaprak et al., 2015). At the same time, it has to be considered how the sample behaves in other applications such as fluorescence microscopy and immuno-labeling. A

considerable amount of attention has to be paid to the fixation and contrasting medium used during freeze-substitution. Since we observed a nice contrast even without the use of OsO_4, we try to reduce the concentration of OsO_4 as much as possible for several reasons. For one, OsO_4 may destroy antibody epitopes. Secondly, the less heavy metal ions are present in the sample the lower the projected mass thickness and the thicker the sections which can be imaged. It may be worthwhile trying to optimize this parameter because it was discussed in the past that biological objects embedded in a resin without any heavy metal yield sufficient contrast in STEM tomography (Engel and Reichelt, 1984; Sousa and Leapman, 2012).

We also noted on several samples that the sectioned surface was not as smooth as desired. It is known that artefacts are introduced during sectioning which e.g. result from the angle of the diamond knife. A

specially designed 35° diamond knife for thick sections may yield a better quality due to its higher stiffness (H. Gnaegi, personal communication).

The true thickness of the sections used in our STEM tomography experiments still remains to be determined. We usually cut sections at a nominal thickness of 800 or 900 nm but this number needs to be taken with some care as our microtomes – although maintained in regular intervals – are not calibrated in terms of absolute section thickness. Furthermore we pre-irradiate our plastic samples before starting the tomography series in order to have a rather constant sample thickness during data collection. We observe a reduction of the thickness of the Epon (in our lab: medium hardness) sections due to electron beam pre-irradiation by ~25% which is in line with previous observations (Kizilyaprak et al., 2015; Luther, 2006). It is important to state that there is a considerable difference between the thickness of the freshly prepared section and that of the section after pre-irradation and during data collection.

4. Materials and methods

4.1. Embedding of tissue

Adult mice were anaesthetized with sodium pentobarbital and perfusion-fixed through the distal abdominal aorta with 2% glutaraldehyde/0.1 M sodium cacodylate pH 7.4 for 3 min. Then kidneys were removed, cut in half and incubated another 2 h in the same solution. Kidney biopsies were high-pressure frozen with EM-PACT2 (Leica, Wetzlar, Germany) and freeze-substituted in acetone/2% OsO_4/5% H_2O/0.25% uranyl acetate using the Leica AFS2, washed in acetone and finally embedded in Epon (Burghardt et al., 2015; Höhn et al., 2011).

4.2. Preparation of sections

Blocks were hardened at 60°C before being trimmed and cut with a diamond knife (histo 45°, or ultra-semi 35°; Diatome, Biel, Switzerland) to obtain 100 nm thick sections and 900 nm thick sections (setting on the microtome; UC6 or UC7, Leica). The thickness of the sections after tomography was determined on the reconstructed three-dimensional volume in IMOD (see below). Sections were mounted on copper grids (50 parallel lines, with or without one single bar across; Plano, Wetzlar, Germany), which were pre-coated with a pioloform film. Grids were additionally covered with a 2.5 to 5 nm thin film of carbon by indirect evaporation, i.e. with the shield in place (Cressington 208 carbon, Watford, England). Conjugates between Protein A and 15 nm gold particles (kindly provided by G. Posthuma, University of Utrecht, NL) were applied as fiducials on both sides of the sections (care was taken to use those particles present in the supernatant of the solution). Finally, the grids were cleaned in a plasma cleaner (2 min, medium power; Harrick Plasma Cleaner PDX) before being mounted in a high-tilt sample holder tip. For recording a dual-axis tomography series we used a dedicated dual-axis holder (Fischione Model 2040; Fischione Germany, Hanau, Germany).

4.3. Set-up and tuning of the transmission electron microscope

For all micrographs and tomograms analyzed in this study, a JEM-2100F transmission electron microscope (JEOL GmbH, Freising, Germany) was operated at 200 kV in STEM mode. For enabling and optimizing the external control of all microscopy parameters, a Universal Scan Generator was installed (TVIPS, Gauting, Germany). In order to enable the analysis of thick samples, our microscope's STEM mode settings were adjusted as follows using free-lens control: spot 1.5 nm; Condensor 1: 30143; Condensor 2: 37919; Condensor Minilens 54544 (the numbers given represent the settings of the lens current). A condensor aperture with a diameter of 20 μm was used to obtain a semi-convergence angle of 1.46 mrad. The diameter of the beam in STEM mode with this setting is ~4 nm as determined from a line scan (full width at half maximum; suppl. Fig. 6). The postmag/descan system of the STEM unit was adjusted such that at 200,000x nominal STEM magnification an area with a size of ~3.5 μm × 3.5 μm could be scanned (lens settings: MagAdj D600/CCC0; Correction 4530/4200). At a camera length of 20 cm, the cutoff of the collection angle between the dark-field and the bright-field detector was at ~28 to 29 mrad. The actual image recorded was 2.74 μm × 2.74 μm (i.e. 2,048 pixels with a pixel size of 1.34 nm).

4.4. Electron tomography

Grids were scanned for suitable specimen areas at a low TEM magnification to allow for a sufficient distance from any grid bars so that a dual-axis dataset could be recorded. Then the sample area was irradiated for about 5 min at a nominal magnification of 2,000x (TEM), to minimize beam-induced shrinkage of the section during the recording of the tilt series (Luther, 2006). TEM images and tomograms were recorded using a F416 CMOS camera (TVIPS, Gauting, Germany). In order to be able to compare TEM and STEM tomograms a TEM magnification was chosen such that similar pixel sizes were obtained (1.4 nm for TEM and 1.34 nm for STEM). For most tilt series (TEM and STEM), the tilt images were recorded in 90 projections with a nominal 2° increment according to the Saxton scheme (Saxton et al., 1984). After switching to STEM mode, settings for tuning the electron beam with a small convergence angle (as given above) were loaded, followed by a brief check of the ronchigram and focus, and insertion of a condensor aperture with a width of 20 μm. At this stage, a low magnification overview of the sample area can be recorded to ensure the suitability for further studies. Tilt series were recorded without dynamic focusing. The maximum range of tilt angles was +/- 72°, in most cases it was +/- 66°. Control of all settings during tomography, including scanning, tracking, focusing and parallel recording of bright-field and dark-field signals from the respective detectors was controlled by EM-tools and EM-Menu (TVIPS, Gauting, Germany). Bright-field and dark-field data were simultaneously recorded and stored as single images (2048 × 2048 pixels, each), with a nominal pixel size of 1.34 nm. These images were converted into one single data stack (tif2mrc, IMOD) and further processed in etomo (IMOD) without binning or with twofold binning. For TEM and STEM tomography data, two modes of processing were applied, manual image alignment and reconstruction using the fiducials for assisted tracking, or a fully automated tomographic reconstruction scheme ('batch tomograms') which includes the merging of tomograms taken at two orthogonal axes (Mastronarde and Held, 2017). No correction of the contrast transfer function (CTF) was performed. The volumes were reconstructed using the weighted back-projection algorithm, the weighted back-projection algorithm with SIRT-like filter (Zeng, 2012) and the SIRT algorithm, all three as implemented in IMOD.

Declaration of Competing Interest

The authors declare that they have no known competing financial interests or personal relationships that could have appeared to

influence the work reported in this paper.

Appendix A. Supplementary data

Supplementary data to this article can be found online at https://doi.org/10.1016/j.jsb.2020.107551.

References

Ader, N.R., Kukulski, W., 2017. triCLEM: Combining high-precision, room temperature CLEM with cryo-fluorescence microscopy to identify very rare events. Methods Cell Biol. 140, 303–320. https://doi.org/10.1016/bs.mcb.2017.03.009.

Alloyeau, D., Ricolleau, C., Oikawa, T., Langlois, C., Le Bouar, Y., Loiseau, A., 2008. STEM nanodiffraction technique for structural analysis of CoPt nanoparticles. Ultramicroscopy 108 (7), 656–662. https://doi.org/10.1016/j.ultramic.2007.10.006.

Aoyama, K., Takagi, T., Hirase, A., Miyazawa, A., 2008. STEM tomography for thick biological specimens. Ultramicroscopy 109 (1), 70–80. https://doi.org/10.1016/j.ultramic.2008.08.005.

Biskupek, J., Leschner, J., Walther, P., Kaiser, U., 2010. Optimization of STEM tomography acquisition–a comparison of convergent beam and parallel beam STEM tomography. Ultramicroscopy 110 (9), 1231–1237. https://doi.org/10.1016/j.ultramic.2010.05.008.

Biyani, N., Righetto, R.D., McLeod, R., Caujolle-Bert, D., Castano-Diez, D., Goldie, K.N., Stahlberg, H., 2017. Focus: the interface between data collection and data processing in cryo-EM. J. Struct. Biol. 198 (2), 124–133. https://doi.org/10.1016/j.jsb.2017.03.007.

Buban, J.P., Ramasse, Q., Gipson, B., Browning, N.D., Stahlberg, H., 2010. High-resolution low-dose scanning transmission electron microscopy. J. Electron Microsc. 59 (2), 103–112. https://doi.org/10.1093/jmicro/dfp052.

Burghardt, T., Hochapfel, F., Salecker, B., Meese, C., Gröne, H.-J., Rachel, R., Wanner, G., Krahn, M.P., Witzgall, R., 2015. Advanced electron microscopic techniques provide a deeper insight into the peculiar features of podocytes. Am. J. Physiol. Renal Physiol. 309 (12), F1082–9. https://doi.org/10.1152/ajprenal.00338.2015.

Bussi, Y., Shimoni, E., Weiner, A., Kapon, R., Charuvi, D., Nevo, R., Efrati, E., Reich, Z., 2019. Fundamental helical geometry consolidates the plant photosynthetic membrane. PNAS 116 (44), 22366–22375. https://doi.org/10.1073/pnas.1905994116.

Davidi, L., Shimoni, E., Khozin-Goldberg, I., Zamir, A., Pick, U., 2014. Origin of β-carotene-rich plastoglobuli in Dunaliella bardawil. Plant Physiol. 164 (4), 2139–2156. https://doi.org/10.1104/pp.113.235119.

Denk, W., Horstmann, H., 2004. Serial block-face scanning electron microscopy to reconstruct three-dimensional tissue nanostructure. PLoS Biol. 2 (11), e329. https://doi.org/10.1371/journal.pbio.0020329.

Engel, A., Reichelt, R., 1984. Imaging of biological structures with the scanning transmission electron microscope. J. Ultrastruct. Res. 88 (2), 105–120. https://doi.org/10.1016/S0022-5320(84)80003-9.

Frank, J., 1992. Electron Tomography: Three-Dimensional Imaging with the Transmission Electron Microscope. Plenum Press, New York, pp. 399.

Ganesh, K.J., Kawasaki, M., Zhou, J.P., Ferreira, P.J., 2010. D-stem: a parallel electron diffraction technique applied to nanomaterials. Microscopy Microanal. 16 (5), 614–621. https://doi.org/10.1017/S1431927610000334.

Hochapfel, F., Denk, L., Maaßen, C., Zaytseva, Y., Rachel, R., Witzgall, R., Krahn, M.P., 2018. Electron microscopy of Drosophila garland cell nephrocytes: optimal preparation, immunostaining and STEM tomography. J. Cell. Biochem. 119 (10), 8011–8021. https://doi.org/10.1002/jcb.26702.

Hohmann-Marriott, M.F., Sousa, A.A., Azari, A.A., Glushakova, S., Zhang, G., Zimmerberg, J., Leapman, R.D., 2009. Nanoscale 3D cellular imaging by axial scanning transmission electron tomography. Nat. Methods 6 (10), 729–731. https://doi.org/10.1038/nmeth.1367.

Höhn, K., Sailer, M., Wang, L., Lorenz, M., Schneider, M.E., Walther, P., 2011. Preparation of cryofixed cells for improved 3D ultrastructure with scanning transmission electron tomography. Histochem. Cell Biol. 135 (1), 1–9. https://doi.org/10.1007/s00418-010-0765-z.

Kizilyaprak, C., Longo, G., Daraspe, J., Humbel, B.M., 2015. Investigation of resins suitable for the preparation of biological sample for 3-D electron microscopy. J. Struct. Biol. 189 (2), 135–146. https://doi.org/10.1016/j.jsb.2014.10.009.

Luther, P.K., 2006. Sample Shrinkage and Radiation Damage of Plastic Sections. In: Frank, J. (Ed.), Electron Tomography. Springer, New York, New York, NY, pp. 17–48.

Markert, S.M., Britz, S., Proppert, S., Lang, M., Witvliet, D., Mulcahy, B., Sauer, M., Zhen, M., Bessereau, J.-L., Stigloher, C., 2016. Filling the gap: adding super-resolution to array tomography for correlated ultrastructural and molecular identification of electrical synapses at the C. elegans connectome. Neurophotonics 3 (4), 41802. https://doi.org/10.1117/1.NPh.3.4.041802.

Mastronarde, D.N., 1997. Dual-axis tomography: an approach with alignment methods that preserve resolution. J. Struct. Biol. 120 (3), 343–352. https://doi.org/10.1006/jsbi.1997.3919.

Mastronarde, D.N., Held, S.R., 2017. Automated tilt series alignment and tomographic reconstruction in IMOD. J. Struct. Biol. 197 (2), 102–113. https://doi.org/10.1016/j.jsb.2016.07.011.

Micheva, K.D., Smith, S.J., 2007. Array tomography: a new tool for imaging the molecular architecture and ultrastructure of neural circuits. Neuron 55 (1), 25–36. https://doi.org/10.1016/j.neuron.2007.06.014.

Mittelberger, A., Kramberger, C., Meyer, J.C., 2018. Software electron counting for low-dose scanning transmission electron microscopy. Ultramicroscopy 188, 1–7. https://doi.org/10.1016/j.ultramic.2018.02.005.

Mutsafi, Y., Shimoni, E., Shimon, A., Minsky, A., 2013. Membrane assembly during the infection cycle of the giant Mimivirus. PLoS Pathog. 9 (5), e1003367. https://doi.org/10.1371/journal.ppat.1003367.

Reimer, L., Kohl, H., 2008. Transmission electron microscopy: Physics of image formation, 5th ed., 587 pp.

Savitzky, B.H., El Baggari, I., Clement, C.B., Waite, E., Goodge, B.H., Baek, D.J., Sheckelton, J.P., Pasco, C., Nair, H., Schreiber, N.J., Hoffman, J., Admasu, A.S., Kim, J., Cheong, S.-W., Bhattacharya, A., Schlom, D.G., McQueen, T.M., Hovden, R., Kourkoutis, L.F., 2018. Image registration of low signal-to-noise cryo-STEM data. Ultramicroscopy 191, 56–65. https://doi.org/10.1016/j.ultramic.2018.04.008.

Saxton, W.O., Baumeister, W., Hahn, M., 1984. Three-dimensional reconstruction of imperfect two-dimensional crystals. Ultramicroscopy 13 (1–2), 57–70. https://doi.org/10.1016/0304-3991(84)90057-3.

Schauflinger, M., Villinger, C., Mertens, T., Walther, P., von Einem, J., 2013. Analysis of human cytomegalovirus secondary envelopment by advanced electron microscopy. Cell. Microbiol. 15 (2), 305–314. https://doi.org/10.1111/cmi.12077.

Sousa, A.A., Azari, A.A., Zhang, G., Leapman, R.D., 2011. Dual-axis electron tomography of biological specimens: extending the limits of specimen thickness with bright-field STEM imaging. J. Struct. Biol. 174 (1), 107–114. https://doi.org/10.1016/j.jsb.2010.10.017.

Sousa, A.A., Leapman, R.D., 2012. Development and application of STEM for the biological sciences. Ultramicroscopy 123, 38–49. https://doi.org/10.1016/j.ultramic.2012.04.005.

Trépout, S., Tassin, A.-M., Marco, S., Bastin, P., 2018. STEM tomography analysis of the trypanosome transition zone. J. Struct. Biol. 202 (1), 51–60. https://doi.org/10.1016/j.jsb.2017.12.005.

Walther, P., Bauer, A., Wenske, N., Catanese, A., Garrido, D., Schneider, M., 2018. STEM tomography of high-pressure frozen and freeze-substituted cells: a comparison of image stacks obtained at 200 kV or 300 kV. Histochem. Cell Biol. 150 (5), 545–556. https://doi.org/10.1007/s00418-018-1727-0.

Williams, D.B., Carter, C.B., 2009. Transmission Electron Microscopy: A Textbook for Materials Science, second ed. Springer, New York, pp. 15.

Wolf, S.G., Houben, L., Elbaum, M., 2014. Cryo-scanning transmission electron tomography of vitrified cells. Nat. Methods 11 (4), 423–428. https://doi.org/10.1038/nmeth.2842.

Wolf, S.G., Mutsafi, Y., Dadosh, T., Ilani, T., Lansky, Z., Horowitz, B., Rubin, S., Elbaum, M., Fass, D., 2017. 3D visualization of mitochondrial solid-phase calcium stores in whole cells. eLife 6. https://doi.org/10.7554/eLife.29929.

Zeng, G.L., 2012. A filtered backprojection algorithm with characteristics of the iterative landweber algorithm. Med. Phys. 39 (2), 603–607. https://doi.org/10.1118/1.3673956.